Bearing Estimation on $\mathbb{S}^2$ via Tangent-Space Measurements for UAV Formation Control

Julio César Rodríguez
Dept. of Electrical Engineering
CINVESTAV Guadalajara
Jalisco, México
julio.rodriguez@cinvestav.mx

Héctor M. Becerra
Dept. of Computer Science
CIMAT
Guanajuato, México
hector.becerra@cimat.mx

Javier Ruiz León
Dept. of Electrical Engineering
CINVESTAV Guadalajara
Jalisco, México
javier.ruiz@cinvestav.mx

***Abstract*—In this paper, two bearing filters on the tangent space of $\mathbb{S}^2$ are proposed for multi-UAV formation control. In multi-agent systems, bearing values obtained usually from raw ArUco/PnP bearing measurements suffer from pixel-level discontinuities, range-dependent noise, and unusable numerical derivatives. To overcome these limitations, we propose in this paper two filters that operate in the local Euclidean tangent plane, recovering a unit-norm estimate via retraction, and jointly estimating bearing, rate, and acceleration without numerical differentiation. The first proposed filter is a tangent-space Kalman filter, and the second one is an H_∞ filter with a minimax energy attenuation bound, providing formal robustness guarantees against any finite-energy disturbance without requiring Gaussian noise assumptions. A distance-dependent noise model and Mahalanobis distance gate (statistical outlier rejection test) handle detection outliers. Gazebo-ROS simulations on Crazyflie nano-quadrotor models show that both filters achieve low mean geodesic error while preserving unit-norm consistency. The H_∞ filter further reduces bearing-rate RMSE relative to the Kalman filter.**

***Index Terms*—Bearing estimation, Kalman filter, H_∞ filter, tangent space, unit sphere $\mathbb{S}^2$, multi-UAV, formation control, ArUco markers.**

I. Introduction

Bearing-only formation control has attracted significant research attention in recent years, particularly within multi-agent systems. In these frameworks, each agent measures the unit direction vector (*bearing*) toward its neighbors, which is then used to achieve a desired formation. However, many foundational works idealize the sensing process and do not address practical issues that arise when bearings are obtained from vision-based systems [1].

A bearing vector is a unit vector constrained to $\mathbb{S}^2 \subset \mathbb{R}^3$ (following the notation of [1]). Because a bearing captures only the direction between agents and not full orientation, it lives on $\mathbb{S}^2$ rather than in $SO(3)$. When fiducial markers such as ArUco [2] are used as visual targets, the Perspective-n-Point (PnP) algorithm recovers the relative pose from pixel corner detections, yielding a raw bearing measurement. In practice, raw ArUco/PnP bearing measurements suffer from three compounding problems detailed in Section II-C: pixel-level discontinuities, range-dependent stochastic noise [3], and unusable numerical derivatives.

Research on state estimation has evolved considerably. Hertzberg et al. [4] established a boxplus/boxminus framework for manifold-compatible fusion; Kotaru and Sreenath [5] developed a variation-based EKF directly on $\mathbb{S}^2$; and Baran and Bergmann [6] unified Lie-group and Riemannian Kalman filters under a single affine-connection framework. For bearing estimation specifically, Serrano et al. [7] proposed an equivariant observer on $\mathbb{S}^2$ assuming known agent velocities; Ramírez-Parada et al. [8] demonstrated vision-based bearing-only formation on real quadrotors; and Zheng et al. [9] optimized spatial-temporal triangulation for cooperative motion estimation. On robustness, Aslam and Haydar [10] derived a nonlinear H_∞ filter on $SO(3)$, and Choukroun et al. [11] extended H_∞ to quaternion attitude estimation. Unlike these works, the filters proposed here require no agent velocity as input measurement, and model PnP noise with a distance-dependent covariance that grows linearly with inter-agent range.

A common alternative is to apply a Kalman filter directly to the three Cartesian components of $\boldsymbol{g}_{ij} \in \mathbb{R}^3$ and renormalize after each update; however, this is geometrically inconsistent: renormalization does not commute with the Kalman update, so the covariance $\mathbf{P}$ no longer represents true estimation uncertainty [4]. The proposed tangent-space formulation resolves both the manifold constraint and the derivative problem without the overhead of full geometric integration. Despite these advances, no existing approach simultaneously handles the $\mathbb{S}^2$ manifold constraint, provides formal robustness against non-Gaussian disturbances, and estimates bearing rate without agent velocity input.

Addressing these gaps, the main contributions of this paper are: (i) a proposed tangent-space Kalman Filter (KF) on $\mathbb{S}^2$ with a 6-state constant-angular-acceleration model that jointly estimates bearing, rate, and acceleration; (ii) a proposed tangent-space H_∞ filter on $\mathbb{S}^2$ with minimax robustness against non-Gaussian disturbances; and (iii) a distance-dependent noise model, Mahalanobis outlier gate, and retraction step that maintain unit-norm consistency, validated in

The first author was supported by the Mexican National Council of Science, Humanities, Technology, and Innovation (SECIHTI), CVU: 1155764.

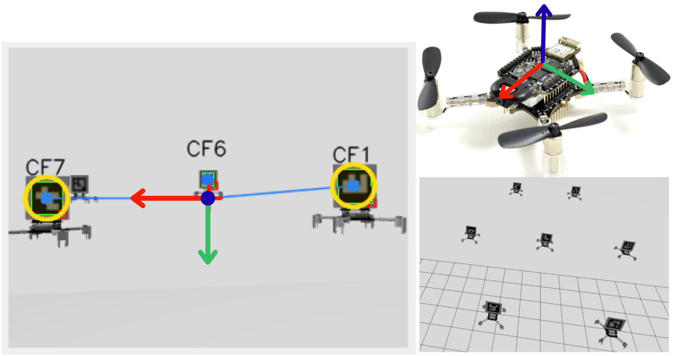

Fig. 1. Body and camera coordinate frames of the Crazyflie platform (left); seven-agent formation in Gazebo under the H_∞ filter (right).

Gazebo-ROS on eight directed formation pairs of Crazyflie nano-quadrotors.

This paper is organized as follows: Section II presents the bearing representation and the ArUco-based measurement process. In Section III, the tangent-space Kalman filter is described, and Section IV develops the H_∞ filter. Section V details the enhancement steps shared by both filters. The simulation results are detailed in Section VI. Finally, Section VII presents the conclusions.

II. Preliminaries

A. Bearing Vector on $\mathbb{S}^2$

The bearing from agent i to agent j, with positions $\mathbf{p}_i, \mathbf{p}_j \in \mathbb{R}^3$, is the unit direction vector $\boldsymbol{g}_{ij} = (\mathbf{p}_j - \mathbf{p}_i)/\|\mathbf{p}_j - \mathbf{p}_i\| \in \mathbb{S}^2$, where $\mathbb{S}^2 \subset \mathbb{R}^3$ is a smooth two-dimensional manifold but not a vector space [4].

B. ArUco-Based Bearing Measurement

In this setting, each agent carries an ArUco marker. The on-board camera detects the four pixel corners $\{(u_i, v_i)\}_{i=1}^4$, and the IPPE variant of `solvePnP` [12] solves:

$$\lambda_i \begin{pmatrix} u_i \\ v_i \\ 1 \end{pmatrix} = \mathbf{K}\,[\,\mathbf{R} \mid \mathbf{t}\,] \begin{pmatrix} \mathbf{P}_i^{\mathcal{M}} \\ 1 \end{pmatrix}, \quad i = 1, \ldots, 4, \tag{1}$$

where $\mathbf{K} \in \mathbb{R}^{3\times3}$ is the camera calibration matrix, $\lambda_i > 0$ is the projective depth of corner i, $\mathbf{R} \in SO(3)$ is the rotation matrix from the marker frame to the camera frame, and $\mathbf{t} \triangleq \mathbf{p}_{j|c} \in \mathbb{R}^3$ is the position of marker j in the camera frame.

The fixed camera-to-robot rotation

$$\mathbf{R}_{c\to r} = \begin{pmatrix} 0 & 0 & 1 \\ -1 & 0 & 0 \\ 0 & -1 & 0 \end{pmatrix} \tag{2}$$

is the extrinsic calibration for the forward-facing camera mounted on the Crazyflie platform, aligning the optical z-axis with the robot's forward x-axis. It gives the position in the robot frame $\mathbf{p}_{j|r} = \mathbf{R}_{c\to r}\,\mathbf{p}_{j|c}$, and the raw measured bearing is $\boldsymbol{z}_{ij} = \mathbf{p}_{j|r}/\left\|\mathbf{p}_{j|r}\right\| \in \mathbb{S}^2$.

Fig. 1 illustrates the extrinsic calibration (2): the left panel shows the camera view of agent 2 with the camera-frame axes at the focal point, and the right panel shows the Crazyflie body frame, with the optical z-axis aligned to the robot's forward x-axis. Each agent is labeled CF N, where N is its ArUco tag identifier; the yellow circle denotes the 2σ bearing uncertainty produced by an estimator (Section III) projected onto the image plane via the pinhole model $r = f_x \tan(2\sigma)$.

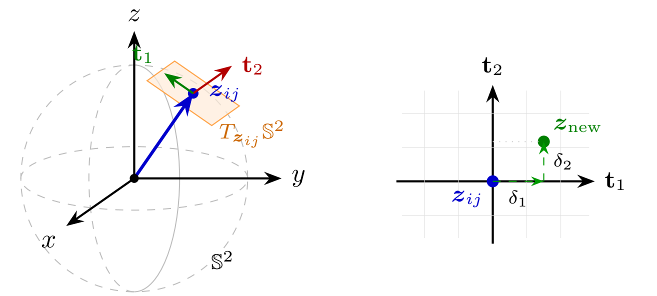

Fig. 2. (Left) Bearing $\boldsymbol{z}_{ij}$ on $\mathbb{S}^2$ and tangent plane $T_{\boldsymbol{z}_{ij}}\mathbb{S}^2$. (Right) Tangent-plane components (δ_1, δ_2) at the reference bearing $\boldsymbol{z}_{ij} \in \mathbb{S}^2$.

C. Limitations of the Raw Measurement

The raw $\boldsymbol{z}_{ij}$ is unsuitable for bearing-only controllers due to pixel-level discontinuities, distance-growing stochastic noise (modeled as $r(d) = r_0 + r_1\left\|\mathbf{p}_{j|r}\right\|$, see Section III), and a numerical derivative with excessive variance that renders it unreliable for direct use in a controller. Applying a KF to the Cartesian components and renormalizing after each update is geometrically inconsistent: renormalization does not commute with the Kalman update [4]. The tangent-space formulation resolves both the manifold constraint and the derivative problem.

III. Tangent Space Kalman Filter Design

A. Tangent Plane and Orthonormal Basis

At any reference bearing $\boldsymbol{z}_{ij} \in \mathbb{S}^2$, the tangent space $T_{\boldsymbol{z}_{ij}}\mathbb{S}^2$ is the two-dimensional plane orthogonal to $\boldsymbol{z}_{ij}$. A pair of orthonormal tangent vectors $\{\mathbf{t}_1, \mathbf{t}_2\}$ spanning $T_{\boldsymbol{z}_{ij}}\mathbb{S}^2$ is constructed as follows. Choose a vector not parallel to $\boldsymbol{z}_{ij}$, e.g. $\mathbf{e}_x = (1,0,0)^\top$ if $|z_{ij,x}| < 0.9$, otherwise $\mathbf{e}_y = (0,1,0)^\top$. Then:

$$\mathbf{t}_1 = \frac{\boldsymbol{z}_{ij} \times \mathbf{e}}{\|\boldsymbol{z}_{ij} \times \mathbf{e}\|}, \tag{3}$$

$$\mathbf{t}_2 = \frac{\boldsymbol{z}_{ij} \times \mathbf{t}_1}{\|\boldsymbol{z}_{ij} \times \mathbf{t}_1\|}. \tag{4}$$

The triplet $\{\boldsymbol{z}_{ij}, \mathbf{t}_1, \mathbf{t}_2\}$ forms an orthonormal frame of $\mathbb{R}^3$; Fig. 2 illustrates the sphere geometry (left) and the tangent-plane displacement components (δ_1, δ_2) (right).

B. State Vector

For each pair of agents (i,j), the filter $\mathcal{F}_{i\to j}$ maintains the state $\mathbf{x} = \left(\delta_1,\, \delta_2,\, \omega_1,\, \omega_2,\, \alpha_1,\, \alpha_2\right)^\top \in \mathbb{R}^6$, where (δ_1, δ_2) is the angular displacement in the tangent plane [rad], (ω_1, ω_2) is the angular velocity [rad/s], and (α_1, α_2) is the angular acceleration [rad/s^2].

C. Process Model

A constant angular-acceleration (CAA) model is adopted. This choice is preferred over a constant-velocity model for two reasons: (i) in formation flight, bearing changes are smooth and the additional degree of freedom improves tracking of non-trivial trajectories; (ii) the acceleration state (α_1, α_2) can serve as a feedforward signal for bearing-only controllers without requiring numerical differentiation. For each tangent axis $\ell \in \{1, 2\}$:

$$\delta_\ell(t+\Delta t) = \delta_\ell + \omega_\ell \Delta t + \tfrac{1}{2}\alpha_\ell \Delta t^2 + w_\ell^\delta, \tag{5}$$

$$\omega_\ell(t+\Delta t) = \omega_\ell + \alpha_\ell \Delta t + w_\ell^\omega, \tag{6}$$

$$\alpha_\ell(t+\Delta t) = \alpha_\ell + w_\ell^\alpha. \tag{7}$$

The noise for axis ℓ is $(w_\ell^\delta, w_\ell^\omega, w_\ell^\alpha)^\top \sim \mathcal{N}(\mathbf{0}, \mathbf{Q}_1(\Delta t))$. The full process noise $\mathbf{w}_k = (w_1^\delta, w_1^\omega, w_1^\alpha, w_2^\delta, w_2^\omega, w_2^\alpha)^\top \in \mathbb{R}^6$ has covariance $\mathbf{Q}(\Delta t) = q\,\mathrm{diag}(\mathbf{Q}_1(\Delta t), \mathbf{Q}_1(\Delta t))$, where $q\,[\mathrm{rad}^2/\mathrm{s}^3]$ is the acceleration noise intensity.

The block-diagonal state transition matrix is:

$$\mathbf{A}(\Delta t) = \mathrm{diag}(\mathbf{A}_1(\Delta t),\ \mathbf{A}_1(\Delta t)), \quad \mathbf{A}_1(\Delta t) = \begin{pmatrix} 1 & \Delta t & \frac{\Delta t^2}{2} \\ 0 & 1 & \Delta t \\ 0 & 0 & 1 \end{pmatrix}. \tag{8}$$

The constant-acceleration shaping matrix [13] is:

$$\mathbf{Q}_1(\Delta t) = \begin{bmatrix} \frac{\Delta t^4}{4} & \frac{\Delta t^3}{2} & \frac{\Delta t^2}{2} \\ \frac{\Delta t^3}{2} & \Delta t^2 & \Delta t \\ \frac{\Delta t^2}{2} & \Delta t & 1 \end{bmatrix}. \tag{9}$$

D. Measurement Model

The raw measurement $\boldsymbol{z}_k \in \mathbb{S}^2$ is projected onto the current tangent plane as $\boldsymbol{z}_{\tan} = \left(\boldsymbol{z}_k^\top \mathbf{t}_1,\, \boldsymbol{z}_k^\top \mathbf{t}_2\right)^\top \in \mathbb{R}^2$. The observation matrix selects the displacement components:

$$\mathbf{H} = \left[\, \mathbf{I}_2 \mid \mathbf{0}_{2\times 4} \,\right] \in \mathbb{R}^{2\times 6}. \tag{10}$$

The measurement noise covariance is distance-dependent, reflecting the degradation of PnP accuracy with range [3]:

$$\mathbf{R}(d) = r(d)\,\mathbf{I}_2, \qquad r(d) = r_0 + r_1 \left\|\mathbf{p}_{j|r}\right\|, \tag{11}$$

with r_0 and r_1 tuned via Bayesian optimization on recorded flight data.

E. Kalman Filter Cycle

At $k = 0$, $\hat{\boldsymbol{g}}_0 = \boldsymbol{z}_0$ and $\mathbf{x}_{0|0} = \mathbf{0}_6$; $\mathbf{P}_{0|0}$ is diagonal with entries scaled to $\sqrt{q}$; both filters share this initialization.

At each time step t_k with measurement $\boldsymbol{z}_k$ (hereafter $\mathbf{A} \triangleq \mathbf{A}(\Delta t)$ and $\mathbf{Q} \triangleq \mathbf{Q}(\Delta t)$ for brevity):

1) Prediction:

$$\mathbf{x}_{k|k-1} = \mathbf{A}\,\mathbf{x}_{k-1|k-1}, \tag{12}$$

$$\mathbf{P}_{k|k-1} = \mathbf{A}\,\mathbf{P}_{k-1|k-1}\,\mathbf{A}^\top + \mathbf{Q}. \tag{13}$$

2) Innovation: The innovation in tangent coordinates is:

$$\mathbf{y}_k = \boldsymbol{z}_{\tan} - \mathbf{H}\,\mathbf{x}_{k|k-1}, \tag{14}$$

with innovation covariance $\mathbf{S}_k = \mathbf{H}\mathbf{P}_{k|k-1}\mathbf{H}^\top + \mathbf{R}_k$. Outlier rejection via a Mahalanobis distance gate is detailed in Section V.

3) State Correction:

$$\mathbf{K}_k = \mathbf{P}_{k|k-1}\,\mathbf{H}^\top\,\mathbf{S}_k^{-1}, \tag{15}$$

$$\mathbf{x}_{k|k} = \mathbf{x}_{k|k-1} + \mathbf{K}_k\,\mathbf{y}_k, \tag{16}$$

$$\mathbf{P}_{k|k} = (\mathbf{I}_6 - \mathbf{K}_k\mathbf{H})\,\mathbf{P}_{k|k-1}\,(\mathbf{I}_6 - \mathbf{K}_k\mathbf{H})^\top + \mathbf{K}_k\,\mathbf{R}_k\,\mathbf{K}_k^\top, \tag{17}$$

where (17) is the Joseph form, preserving symmetry and positive semi-definiteness of $\mathbf{P}$ under finite-precision arithmetic.

After each update, the retraction and tangent-plane recentering of Section V is applied, restoring the filter reference to the corrected bearing on $\mathbb{S}^2$.

F. Bearing Derivative Estimate

The geometric constraint $\boldsymbol{g}_{ij}^\top \dot{\boldsymbol{g}}_{ij} = 0$ is satisfied by construction. From the filter state:

$$\dot{\hat{\boldsymbol{g}}}_{ij} = \left(\mathbf{I}_3 - \hat{\boldsymbol{g}}_{ij}\hat{\boldsymbol{g}}_{ij}^\top\right)\left(\omega_1\,\mathbf{t}_1 + \omega_2\,\mathbf{t}_2\right), \tag{18}$$

where the projector is included for numerical robustness (in exact arithmetic $\omega_1\mathbf{t}_1 + \omega_2\mathbf{t}_2$ already lies in $T_{\hat{\boldsymbol{g}}}\mathbb{S}^2$). This avoids numerical differentiation.

IV. H_∞ Bearing Filter on $\mathbb{S}^2$

The tangent-space KF of Section III is optimal under Gaussian noise. In practice, nano-quadrotor platforms are subject to propeller vibrations and aerodynamic gusts; outlier measurements might appear that violate this assumption. The H_∞ filter addresses this with a minimax criterion: instead of minimizing expected squared error, it bounds the worst-case energy ratio between estimation error and disturbance to a prescribed level γ^2 [14], [15]. Unlike the equivariant observer of [7] used for bearing estimation, it does not require agent velocity as a measured input and provides formal robustness guarantees against non-Gaussian finite-energy disturbances.

A. Minimax Robustness Criterion

Let $\mathbf{w}_k \in \mathbb{R}^6$ be the process noise vector defined in (5)–(7), and $\mathbf{e}_k = \mathbf{x}_k - \hat{\mathbf{x}}_k$ be the estimation error. The H_∞ criterion requires:

$$\sup_{\mathbf{w}\neq\mathbf{0}} \frac{\sum_{k=0}^{N} \mathbf{e}_k^\top \mathbf{L}\mathbf{e}_k}{\sum_{k=0}^{N} \|\mathbf{w}_k\|^2} < \gamma^2, \tag{19}$$

where $\gamma > 0$ is the prescribed attenuation level and $\mathbf{L} \succeq 0$ is the performance output matrix (detailed in (21)). No statistical characterization of $\mathbf{w}$ is required; the bound holds for any finite-energy disturbance. As $\gamma \to \infty$, the H_∞ filter converges to the Kalman filter (Section IV-C) [15].

B. Modified Riccati Equation

Given $\mathbf{P}_{k|k-1}$ from (13), define:

$$\mathbf{M}_k = \mathbf{P}_{k|k-1}^{-1} - \frac{1}{\gamma^2}\mathbf{L} + \mathbf{H}^\top \mathbf{R}_k^{-1}\mathbf{H}, \tag{20}$$

where $\mathbf{H}$ and $\mathbf{R}_k$ are as in (10) and (11). The performance output matrix is diagonal with tunable weights:

$$\mathbf{L} = \mathrm{diag}\big(\ell_\delta,\, \ell_\delta,\, \ell_\omega,\, \ell_\omega,\, \ell_\alpha,\, \ell_\alpha\big), \tag{21}$$

penalizing position, velocity, and acceleration errors independently. The term $-\gamma^{-2}\mathbf{L}$ is the *adversarial correction*: it makes $\mathbf{P}_{k|k}^{\infty}$ more conservative than the Kalman posterior, which provides the robustness guarantee (19). The updated covariance and gain matrices are given by:

$$\mathbf{P}_{k|k}^{\infty} = \mathbf{M}_k^{-1}, \tag{22}$$

$$\mathbf{K}_k^{\infty} = \mathbf{P}_{k|k}^{\infty}\,\mathbf{H}^\top\,\mathbf{R}_k^{-1}. \tag{23}$$

C. Existence Condition and KF Equivalence

The H_∞ solution exists if and only if $\mathbf{M}_k \succ 0$. In our implementation, this is verified by checking $\lambda_{\min}(\mathbf{M}_k) > 10^{-6}$; if violated, the Kalman gain (15) is used as fallback. This fallback was never triggered for $\gamma \geq 1.5$ in any reported experiment.

KF equivalence follows directly from (20): as $\gamma^{-2} \to 0$, $\mathbf{M}_k \to \mathbf{P}_{k|k-1}^{-1} + \mathbf{H}^\top\mathbf{R}_k^{-1}\mathbf{H}$, and the matrix inversion lemma applied to $\mathbf{M}_k^{-1}$ recovers the standard Kalman posterior covariance and gain.

D. H_∞ Filter Cycle

The prediction (12)–(13) and the innovation (14) are as in Section III; the Mahalanobis gate and retraction are the shared steps of Section V. Only the correction equations change:

$$\mathbf{K}_k^{\infty} = \mathbf{P}_{k|k}^{\infty}\,\mathbf{H}^\top\,\mathbf{R}_k^{-1}, \tag{24}$$

$$\mathbf{x}_{k|k} = \mathbf{x}_{k|k-1} + \mathbf{K}_k^{\infty}\,\mathbf{y}_k, \tag{25}$$

followed by the retraction-recentering (Section V) and bearing derivative (18), both unchanged.

E. Parameter Optimization

The five parameters $(\gamma, q, r_0, r_1, \ell_\omega/\ell_\delta, \ell_\alpha/\ell_\delta)$ are jointly optimized via Bayesian search [16] on the same ROS 2/Gazebo dataset described in Section VI. The dataset spans 50 s at 15 Hz over 0.4–0.9 m inter-agent distances. The objective minimizes the mean angular error $\bar{e} = \frac{1}{N}\sum_k \arccos(\hat{\boldsymbol{g}}_k^\top \boldsymbol{g}_k^{\mathrm{GT}})$, excluding the first 5 s warm-up. Search bounds: $\gamma \in [1.5, 5.0]$, $q \in [10^{-4}, 1]$, $r_0, r_1 \in [10^{-4}, 0.1]$, $\ell_\omega/\ell_\delta, \ell_\alpha/\ell_\delta \in [0.01, 1]$. The optimal $\gamma^* \approx 4.6024$ indicates robust-mode operation, consistent with the non-Gaussian nano-quadrotor environment; re-optimizing over a widened range $\gamma \in [1.5, 10.0]$ yields $\gamma^* \approx 4.62$, confirming that the optimum is interior rather than boundary-constrained. Table I lists all optimized parameters.

V. Enhancement Steps

Both the KF (Section III) and the H_∞ filter (Section IV) incorporate the following two steps after each measurement update.

TABLE I
FILTER PARAMETERS.

Symbol	Description	KF	H_∞
q	Process noise [rad^2/s^3]	0.02120	0.1986
r_0	Noise base [rad^2]	0.001122	0.001122
r_1	Noise scale [rad^2/m]	$3.7768e-05$	$3.7768e-05$
γ	Attenuation level	—	4.6024
ℓ_δ	Position weight	—	1.6759
ℓ_ω	Velocity weight	—	0.2025
ℓ_α	Acceleration weight	—	0.5953

A. Mahalanobis Outlier Gate

At each step, the Mahalanobis distance of the innovation $\mathbf{y}_k$ (14) is computed:

$$d_M = \sqrt{\mathbf{y}_k^\top \mathbf{S}_k^{-1}\mathbf{y}_k} \;>\; \gamma_{\mathrm{gate}} = \begin{cases} 6.0 & n_{\mathrm{upd}} < 8, \\ 3.5 & \text{otherwise}, \end{cases} \tag{26}$$

where n_{upd} is the count of accepted measurements so far. If $d_M > \gamma_{\mathrm{gate}}$, the measurement is discarded and the state is propagated without update ($\mathbf{x}_{k|k} = \mathbf{x}_{k|k-1}$, $\mathbf{P}_{k|k} = \mathbf{P}_{k|k-1}$); otherwise the correction step proceeds and n_{upd} is incremented. During warm-up ($n_{\mathrm{upd}} < 8$), the prior covariance $\mathbf{P}_{k|k-1}$ has not yet contracted from its initial value, making $\mathbf{S}_k$ unreliable; the loose threshold 6.0 prevents premature rejection of measurements needed for convergence. The steady-state value $\gamma_{\mathrm{gate}} = 3.5$ corresponds to the 99.78% percentile of χ_2^2 ($P(d_M < 3.5) = 1 - e^{-6.125} \approx 0.9978$).

B. Retraction and Tangent-Plane Recentering

After correction, the non-zero displacement (δ_1, δ_2) introduces a linearization error. The retraction step recenters the tangent plane at the corrected bearing.

Step 1 — Recover bearing in $\mathbb{R}^3$:

$$\boldsymbol{z}_{\mathrm{new}} = \frac{\boldsymbol{z}_{ij} + \delta_1\,\mathbf{t}_1 + \delta_2\,\mathbf{t}_2}{\|\boldsymbol{z}_{ij} + \delta_1\,\mathbf{t}_1 + \delta_2\,\mathbf{t}_2\|} \;\in\; \mathbb{S}^2. \tag{27}$$

The division by the norm provides explicit renormalization, guaranteeing $\|\boldsymbol{z}_{\mathrm{new}}\| = 1$ exactly at every step. This expression is a first-order approximation of the Riemannian exponential map on $\mathbb{S}^2$; the deviation from the exact map is $O(\|\mathbf{v}\|^3)$, where $\mathbf{v} = \delta_1\mathbf{t}_1 + \delta_2\mathbf{t}_2$, for small tangent corrections.

Step 2 — Lift velocity and acceleration to $\mathbb{R}^3$: $\boldsymbol{\omega} = \omega_1\mathbf{t}_1 + \omega_2\mathbf{t}_2$ and $\boldsymbol{\alpha} = \alpha_1\mathbf{t}_1 + \alpha_2\mathbf{t}_2$.

Step 3 — Update reference and rebuild basis: Set $\boldsymbol{z}_{ij} \leftarrow \boldsymbol{z}_{\mathrm{new}}$, recompute $\{\mathbf{t}_1', \mathbf{t}_2'\}$ via (3)–(4), and re-express the state:

$$\delta_1 = \delta_2 = 0, \quad \omega_i' = \boldsymbol{\omega}^\top\mathbf{t}_i', \quad \alpha_i' = \boldsymbol{\alpha}^\top\mathbf{t}_i'. \tag{28}$$

After recentering, the filter always operates near the tangent-plane origin, keeping the linear approximation valid.

VI. Simulation Results

A. Setup

Both filters were evaluated on a ROS 2/Gazebo simulation with Crazyflie 2.1 nano-quadrotors, equipped with a forward-facing camera (320×240 px, $\mathrm{FOV}_h = 66°$, $f_x{=}f_y{\approx}246.4$ px) and ArUco markers of side $L = 0.045$ m. The seven-agent swarm is split into three leaders (CF1, CF4, CF7)

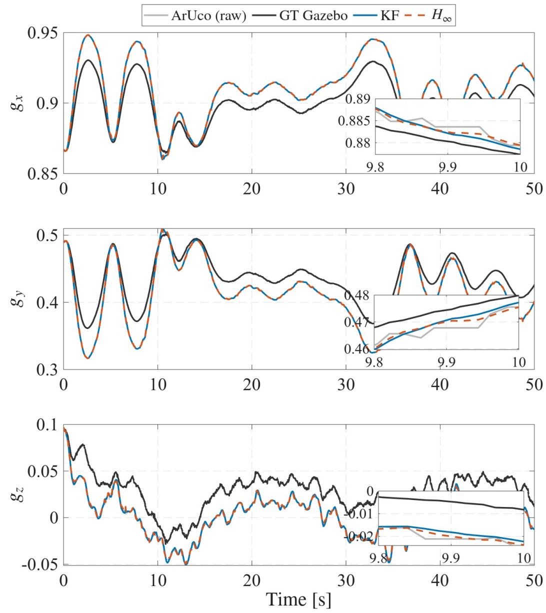

Fig. 3. Bearing components: raw ArUco, ground truth, KF and H_∞ estimates (CF2→CF7).

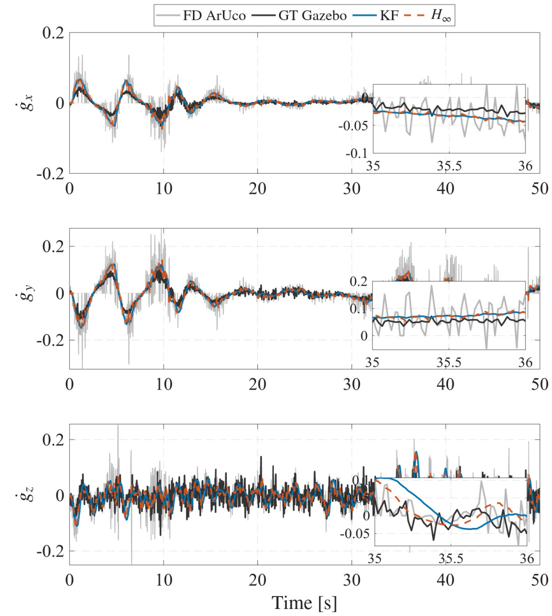

Fig. 4. Bearing-rate: finite differences, ground truth, KF and H_∞ estimates (CF2→CF7).

and four followers (CF2, CF3, CF5, CF6), forming eight directed bearing pairs. Each leader agent executes a sinusoidal trajectory (amplitude $0.5\,\mathrm{m}$, $0.02\,\mathrm{Hz}$) at $0.05\,\mathrm{m/s}$; inter-agent distances range from approximately 0.4 to $0.9\,\mathrm{m}$ during the run. Throughout the run, Gazebo injects stochastic wind gusts on each vehicle, a non-Gaussian, finite-energy disturbance matching the H_∞ design assumption (Section IV). Bearing measurements are generated at $15\,\mathrm{Hz}$ to match the camera frame rate of the physical platform. The comparison between KF and H_∞ was performed offline: raw bearing measurements were logged during the Gazebo run and both filters were applied independently to the same recorded data.

Since the ArUco marker is offset from the vehicle's center of mass, the CoM-based ground truth and the PnP-measured bearing differ geometrically; this offset is estimated from the first sample and subtracted so that $e_k = \arccos(\hat{\boldsymbol{g}}_k^\top \boldsymbol{g}_k^{\mathrm{GT,off}})$ reflects estimation accuracy and avoids a systematic bias of $\approx$0.09 rad.

B. Results

Figures 3 and 4 show the bearing components and bearing-rate estimates for the CF2→CF7 pair. Both filters track the ground truth closely with comparable performance; in the bearing-rate estimates, the H_∞ filter generates a slightly smoother signal relative to the KF, consistent with its minimax energy attenuation design.

Table II reports steady-state metrics for the four directed pairs targeting CF7 (the common leader observed by CF2, CF3, CF5, CF6), where RMSE_e uses marker-offset-corrected ground truth and $\Delta_{\dot{g}}$ is the $\mathrm{RMSE}_{\dot{g}}$ improvement of H_∞ over KF.

Across all pairs, RMSE_e remains below $0.039\,\mathrm{rad}$ for both filters despite the non-Gaussian wind-gust disturbances injected throughout the run. The KF and H_∞ reach comparable RMSE_e ($\Delta < 0.3\%$); however, H_∞ reduces $\mathrm{RMSE}_{\dot{g}}$ by 12–17% under these same disturbances, reflecting the tighter minimax energy bound on the velocity state. The steady-state $\mathrm{tr}(\mathbf{P})$ of the H_∞ filter ($\approx$5.77) is larger than the KF ($\approx$0.69), reflecting the minimax design's deliberate retention of uncertainty to guarantee worst-case robustness. Figures 5 and 6 show the time-evolution of the geodesic and bearing-rate errors for all four pairs.

TABLE II
ESTIMATOR PERFORMANCE, FOUR PAIRS TARGETING CF7 ($t \geq 5$ s, $N = 2426$).

Pair	Estimator	RMSE_e [rad]	$\mathrm{RMSE}_{\dot{g}}$ [rad/s]	$\Delta_{\dot{g}}$ [%]
CF2→CF7	KF	0.0382	0.0419	11.7
	H_∞	**0.0381**	**0.0370**	
CF3→CF7	KF	0.0380	0.0472	13.7
	H_∞	**0.0378**	**0.0407**	
CF5→CF7	KF	0.0365	0.0416	17.0
	H_∞	**0.0364**	**0.0346**	
CF6→CF7	KF	0.0363	0.0431	16.1
	H_∞	**0.0361**	**0.0362**	

These results were obtained under the non-Gaussian wind-gust disturbances of Section VI, not a Gaussian benchmark; the minimax criterion provides formal worst-case guarantees that the KF cannot offer, which explains the observed H_∞ advantage under this adverse, finite-energy disturbance. ArUco marker detection losses caused by limited camera resolution, poor lighting, and unfavorable viewing angles introduce additional non-Gaussian, intermittent measurement noise, an effect expected to be even more pronounced under real flight conditions.

Closed-loop Gazebo trials confirm these trends: H_∞ reduces $\mathrm{RMSE}_{\dot{g}}$ by 12–18% relative to KF across all eight directed

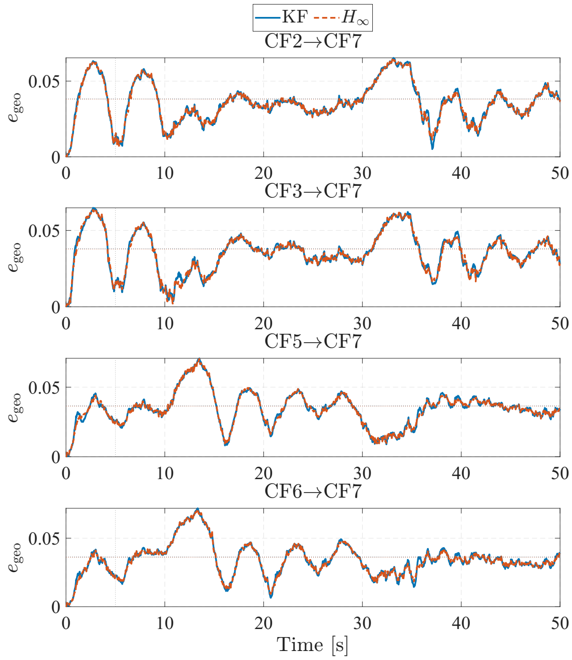

Fig. 5. Geodesic bearing error e_k for the four pairs targeting CF7.

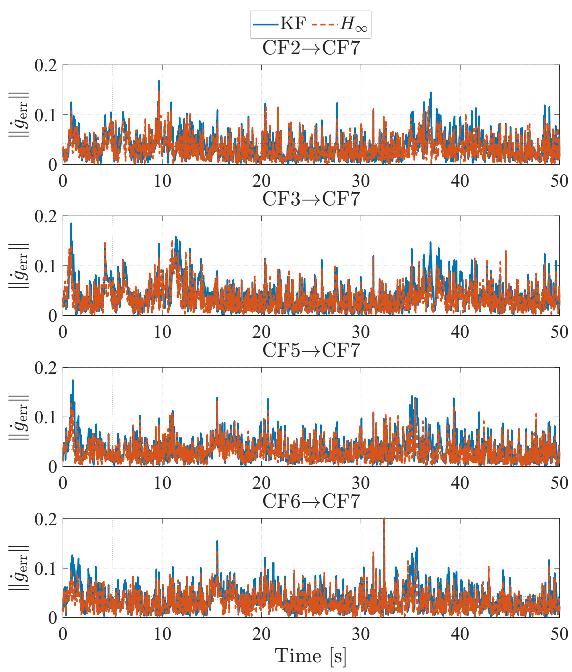

Fig. 6. Bearing-rate error $\|\hat{\dot{\boldsymbol{g}}}_k - \dot{\boldsymbol{g}}_k^{\mathrm{GT}}\|$ for the four pairs targeting CF7.

pairs, with comparable geodesic error. Both filters provided estimates suitable to drive a formation controller without divergence (Fig. 1). A video demonstration is available at https://youtu.be/dzzxMoOREIw.

VII. Conclusions

Two bearing filters on the tangent space of $\mathbb{S}^2$ were proposed for multi-UAV formation control. Both filters apply linear filtering in the local Euclidean tangent plane, recover a unit-norm estimate via retraction, and jointly estimate bearing, rate, and acceleration without numerical differentiation, avoiding full Lie-group overhead. The H_∞ filter additionally provides formal robustness guarantees against any finite-energy disturbance without requiring knowledge of noise statistics — desirable for nano-quadrotor platforms subject to aerodynamic disturbances. Gazebo-ROS simulations under non-Gaussian wind-gust disturbances show that the H_∞ filter attains the best overall bearing and bearing-rate accuracy, confirming its practical advantage over the Kalman filter; both estimators nonetheless provide suitable bearing information for a formation controller to keep a desired geometric pattern. Future work includes real-flight validation on physical Crazyflie platforms and integration with robust formation control strategies under real sensor and actuation conditions.

References

[1] S. Zhao and D. Zelazo, "Bearing rigidity and almost global bearing-only formation stabilization," *IEEE Transactions on Automatic Control*, vol. 61, no. 5, pp. 1255–1268, 2016.

[2] S. Garrido-Jurado, R. Muñoz-Salinas, F. Madrid-Cuevas, and M. Marín-Jiménez, "Automatic generation and detection of highly reliable fiducial markers under occlusion," *Pattern Recognition*, vol. 47, no. 6, pp. 2280–2292, 2014.

[3] A. Marut, K. Wojtowicz, and K. Falkowski, "Aruco markers pose estimation in uav landing aid system," in *2019 IEEE 5th International Workshop on Metrology for AeroSpace (MetroAeroSpace)*, 2019, pp. 261–266.

[4] C. Hertzberg, R. Wagner, U. Frese, and L. Schröder, "Integrating generic sensor fusion algorithms with sound state representations through encapsulation of manifolds," *Information Fusion*, vol. 14, no. 1, pp. 57–77, 2013.

[5] P. Kotaru and K. Sreenath, "Variation based extended kalman filter on s^2," in *2019 18th European Control Conference (ECC)*, 2019, pp. 875–882.

[6] M. Baran and R. Bergmann, "A geometric perspective of state estimation using kalman filters," 2025.

[7] G. Serrano, M. Jacinto, B. J. Guerreiro, and R. Cunha, "Equivariant observer for bearing estimation with linear and angular velocity inputs," *arXiv preprint arXiv:2512.14451*, 2025, submitted to the 2026 European Control Conference.

[8] D. L. Ramírez-Parada, H. M. Becerra, C. A. Toro-Arcila, and G. Arechavaleta, "Vision-based formation control of quadrotors using a bearing-only approach," *Robotics*, vol. 13, no. 8, 2024.

[9] C. Zheng, Y. Mi, H. Guo, H. Chen, Z. Lin, and S. Zhao, "Optimal spatial–temporal triangulation for bearing-only cooperative motion estimation," *Automatica*, vol. 175, p. 112216, 2025.

[10] F. Aslam and M. F. Haydar, "Nonlinear h_∞ filtering on the special orthogonal group $so(3)$ using vector directions," *IEEE Control Systems Letters*, vol. 6, pp. 2599–2604, 2022.

[11] D. Choukroun, L. Cooper, and N. Berman, "Stochastic h_∞ filtering of the attitude quaternion," *Sensors*, vol. 24, no. 24, 2024.

[12] Y. Ma, S. Soatto, J. Košecká, and S. S. Sastry, *An Invitation to 3-D Vision: From Images to Geometric Models*. New York, NY: Springer, 2004.

[13] Y. Bar-Shalom, X. R. Li, and T. Kirubarajan, *Estimation with Applications to Tracking and Navigation*. New York, NY: Wiley-Interscience, 2001.

[14] U. Shaked and Y. Theodor, "h_∞-optimal estimation: a tutorial," in *[1992] Proceedings of the 31st IEEE Conference on Decision and Control*, 1992, pp. 2278–2286.

[15] B. Hassibi, A. H. Sayed, and T. Kailath, *Indefinite-Quadratic Estimation and Control: A Unified Approach to H^2 and H^∞ Theories*. Philadelphia, PA: SIAM, 1999.

[16] T. Akiba, S. Sano, T. Yanase, T. Ohta, and M. Koyama, "Optuna: A next-generation hyperparameter optimization framework," in *Proceedings of the 25th ACM SIGKDD International Conference on Knowledge Discovery & Data Mining*, ser. KDD '19. New York, NY, USA: Association for Computing Machinery, 2019, pp. 2623–2631.